

Investigation of helicity-dependent photocurrent of surface states in(Bi0.7Sb0.3)2Te3 nanoplate

Qin Yu(喻钦), Jinling Yu(俞金玲), Yonghai Chen(陈涌海), Yunfeng Lai(赖云锋), Shuying Cheng(程树英), and Ke He(何珂)

Citation: Chin. Phys. B, 2024, 33 (**5**): 057101. DOI: 10.1088/1674-1056/ad322c
Journal homepage: http://cpb.iphy.ac.cn; http://iopscience.iop.org/cpb

What follows is a list of articles you may be interested in

Highly anisotropic Dirac fermion and spin transportproperties in Cu-graphane

Chao Wu(吴超), Lichuan Zhang(张礼川), Lin Xia(夏霖), Dong Hao(郝东), Shiqi Li(李仕琪), Lizhi Zhang(张礼智), Yuee Xie(谢月娥), and Yuanping Chen(陈元平)
Chin. Phys. B, 2023, 32 (**8**): 087104. DOI: 10.1088/1674-1056/accff1

Rashba spin-orbit coupling induced rectified currents in monolayer graphene with exchange field and sublattice potential

Liang Chen(陈亮), Feng Li(李峰), and Xiao-Ming Ding(丁晓明)
Chin. Phys. B, 2023, 32 (**8**): 087103. DOI: 10.1088/1674-1056/acc932

Topological properties of Sb(111) surface: A first-principles study

Shuangxi Wang(王双喜) and Ping Zhang(张平)
Chin. Phys. B, 2022, 31 (**4**): 047105. DOI: 10.1088/1674-1056/ac46bc

SU(3) spin-orbit coupled fermions in an optical lattice

Xiaofan Zhou(周晓凡), Gang Chen(陈刚), and Suo-Tang Jia(贾锁堂)
Chin. Phys. B, 2022, 31 (**1**): 017102. DOI: 10.1088/1674-1056/ac11dc

Review of Raman spectroscopy of two-dimensional magnetic van der Waals materials

Yu-Jia Sun(孙宇伽), Si-Min Pang(庞思敏), and Jun Zhang(张俊)
Chin. Phys. B, 2021, 30 (**11**): 117104. DOI: 10.1088/1674-1056/ac1e0f

---

Investigation of helicity-dependent photocurrent of surface states in $(Bi_{0.7}Sb_{0.3})_2Te_3$ nanoplate

Qin Yu(喻钦)[1], Jinling Yu(俞金玲)[1,2,†], Yonghai Chen(陈涌海)[3], Yunfeng Lai(赖云锋)[1], Shuying Cheng(程树英)[1,4], and Ke He(何珂)[5]

[1] *School of Advanced Manufacturing, Fuzhou University, Quanzhou* 362251, *China*
[2] *Institute of Micro/Nano Devices and Solar Cells, School of Physics and Information Engineering, Fuzhou University, Fuzhou* 350108, *China*
[3] *Key Laboratory of Semiconductor Materials Science, Institute of Semiconductors, Chinese Academy of Sciences, Beijing* 100083, *China*
[4] *Jiangsu Collaborative Innovation Center of Photovolatic Science and Engineering, Changzhou University, Changzhou* 213164, *China*
[5] *Department of Physics, State Key Laboratory of Low Dimensional Quantum Physics, Tsinghua University, Beijing* 100084, *China*

(Received 7 January 2024; revised manuscript received 17 February 2024; accepted manuscript online 11 March 2024)

Helicity-dependent photocurrent (HDPC) of the surface states in a high-quality topological insulator $(Bi_{0.7}Sb_{0.3})_2Te_3$ nanoplate grown by chemical vapor deposition (CVD) is investigated. By investigating the angle-dependent HDPC, it is found that the HDPC is mainly contributed by the circular photogalvanic effect (CPGE) current when the incident plane is perpendicular to the connection of the two contacts, whereas the circular photon drag effect (CPDE) dominates the HDPC when the incident plane is parallel to the connection of the two contacts. In addition, the CPGE of the $(Bi_{0.7}Sb_{0.3})_2Te_3$ nanoplate is regulated by temperature, light power, excitation wavelength, the source–drain and ionic liquid top-gate voltages, and the regulation mechanisms are discussed. It is demonstrated that $(Bi_{0.7}Sb_{0.3})_2Te_3$ nanoplates may provide a good platform for novel opto-spintronics devices.

Keywords: $(Bi_{0.7}Sb_{0.3})_2Te_3$ nanoplate, helicity-dependent photocurrent, circular photogalvanic effect, ionic liquid gating

PACS: 71.70.Ej, 72.25.Fe, 75.70.Tj, 75.76.+j **DOI:** 10.1088/1674-1056/ad322c

1. Introduction

Spintroninc s have attracted much research interests since it has lots of advantages compared with conventional electronics.[1–5] One of the key aspects of spintronics is the generation, manipulation and detection of the spin of electrons. Spin–orbit coupling (SOC) provides an important way to generate or control the spin of electrons via electrical methods.[3,6–8] Three-dimensional (3D) topological insulators (TIs) have spin-momentum locked surface states, which possess large SOC and become good candidates for designing spintroninc devices.[1,6,9–13]

Helicity dependent photocurrent (HDPC) is an important method to investigate the surface states of 3D TIs, and it has been used to explore the properties of the surface states of Bi_2Se_3 thin films and nanoplates, Bi_2Te_3 thin films, Sb_2Te_3 and $(Bi_{1-x}Sb_x)_2Te_3$ thin films.[4,14–17] Besides, the HDPC can further expand the versatility of the charge–spin interchange in the topological insulator by utilizing the polarization of photons.[18] The influence of the position of Fermi level and excitation wavelength on HDPC of $(Bi_{1-x}Sb_x)_2Te_3$ thin films have been investigated, and it is revealed that the HDPC achieves a maximum value when the Fermi level is set near the Dirac point.[4,18] However, there is no reports investigating the HDPC of $(Bi_{1-x}Sb_x)_2Te_3$ nanoplates. Since nanoplates have larger surface-to-volume ratio, it is expected that nanoplates can more effectively utilize the surface states and the nanoplate device may show better performance compared with that made of thin films. Besides, HDPC can be attributed to the two main mechanisms, i.e., the circular photogalvanic effect (CPGE) and circular photon drag effect (CPDE).[11,19–22] The influence of the light incident plane on the dominant mechanisms of the HDPC for 3D TI nanoplates is still unclear.

In this paper, the HDPC of the surface states in a $(Bi_{0.7}Sb_{0.3})_2Te_3$ nanoplate is systematically investigated. When the incident plane of the light is perpendicular to the connection of the two contacts, the HDPC shows an odd function of incident angles, and it is found that under this case the CPGE plays the dominant role. When the incident plane of the light is parallel to the connection of the two contacts, the HDPC shows an even function of incident angles, indicating that the CPDE makes a major contribution. Finally, we also tune the CPGE current by temperature, light power, excitation wavelength, source–drain voltages and ionic liquid top-gate voltages, and the underlying physical mechanisms are discussed.

2. Experimental details

$(Bi_{0.7}Sb_{0.3})_2Te_3$ nanoplates were grown on SiO_2/(100) Si substrates by CVD method. 20 mg of Sb_2Te_3 powder (99.999%, Alfa Aesar) and 20 mg of Bi_2Te_3 powder

†Corresponding author. E-mail: jlyu@semi.ac.cn

© 2024 Chinese Physical Society and IOP Publishing Ltd

(99.999%, Alfa Aesar) were placed 20 cm and 10 cm, respectively, upside of the furnace center. The SiO_2/Si substrates were placed in the downstream with a distance of 10 cm to 12 cm from the furnace center, as shown in Fig. 1(a). During the growth of the nanoplates, the pressure of the tube was kept at 25 Pa, and Ar with a flow rate of 30 standard cubic centimeters (sccm) was used as a carrier gas. The furnace was heated up to 430 °C within 30 min, and kept at 430 °C for 150 min. After that, the system was naturally cooled down to room temperature under the Ar atmosphere. Then the $(Bi_{0.7}Sb_{0.3})_2Te_3$ nanoplates were mechanically transferred to a clean SiO_2/(100) Si substrate. By using the CVD method, the key factors to determine the ratio of elements in the nanoplates are the temperature and the distance between the source materials and the substrates. Since the two different materials Sb_2Te_3 and Bi_2Te_3 have different evaporation rates at a certain temperature, the final ratio of elements in the nanoplate may not equal to the molar ratio of the source materials. In our experiment, under the growth parameters mentioned above, the element ratio of Sb to Bi in the $(Bi_{1-x}Sb_x)_2Te_3$ nanoplate is 3 to 7, measured by the energy dispersive x-ray spectroscopy (EDS). The standard lithography was used to prepare resist masks of contacts on top of the nanoplate, and then 80-nm Au was deposited by thermal evaporation followed by the standard liftoff procedures. The distance between the two Au contacts was about 5 μm.

A scanning electron microscope (SEM, Quanta 250) was used to analyze the morphology of the nanoplate. An EDS system was used to analyzed the element components of the nanoplate. A Raman spectrometer (Renishaw invia Reflex) with an excitation laser of 532 nm was used to analyzed the structural properties of the nanoplate. A atomic force microscope (AFM, Bruker ICON) was used to measure the thickness and surface roughness of the nanoplate. For HDPC measurement, a solid state laser of 1064 nm was used as the light source. The laser sequentially passed through a chopper, a polarizer, a quarter-wave plate, a lens with a focus of 20 mm, and then illuminated on the sample with a light spot of about 300 μm in diameter, as shown in Fig. 2(a). The photocurrent was collected by the two contacts, and then amplified by a pre-amplifier and a lock-in amplifier. The reference frequency of the lock-in amplifier came from the chopper, which was 229 Hz. To prevent the degradation of the sample, the sample was mounted in an optical cryostat with a low pressure of 1 Pa.

3. Results and discussion

Figure 1(b) shows the SEM image of the $(Bi_{1-x}Sb_x)_2Te_3$ nanoplate. Figures 1(c)–1(e) display the elemental mapping of Te, Bi, and Sb, measured by the EDS provided by SEM. It can be seen that the elements are distributed uniformly in the nanoplate. The EDS spectrum of the $(Bi_{1-x}Sb_x)_2Te_3$ nanoplate is shown in Fig. 1(f), from which the atomic ratio of Bi, Te and Sb are estimated to be 29%±5%, 13%±5%, and 58%±4%, respectively. Therefore, x in the $(Bi_{1-x}Sb_x)_2Te_3$ nanoplate can be estimated to be 0.3. The thickness of the nanoplate is measured by the AFM to be about 30 nm with a surface roughness of 0.6 nm.

Figure 1(f) shows the Raman spectrum of the $(Bi_{0.7}Sb_{0.3})_2Te_3$ nanoplate. It can be seen that the Raman spectrum exhibits four active modes located at about 91 cm^{-1}, 100 cm^{-1}, 121 cm^{-1}, and 141 cm^{-1}, respectively, which can be attributed to the A_{1g}^1, A_{1u}^1, E_g^2, and A_{1g}^2 modes.[19] A_{1g}^1 and A_{1g}^2 modes are due to the out-of-plane vibrations of Bi/Sb–Te pairs, and E_g^2 mode arises from the in-plane vibration of Bi/Sb–Te pairs.[19] The A_{1u}^1 is an infrared active mode, and its presence is because of the different ionic sizes of the Bi, Sb, and Te atoms or may be due to the particle size effect of the $(Bi_{0.7}Sb_{0.3})_2Te_3$.[19] The Raman peak positions are consistent with that observed in the $(Bi_{0.7}Sb_{0.3})_2Te_3$ powder sample reported in Ref. [19], confirming that the synthesized nanoplate is indeed $(Bi_{0.7}Sb_{0.3})_2Te_3$ nanoplate.

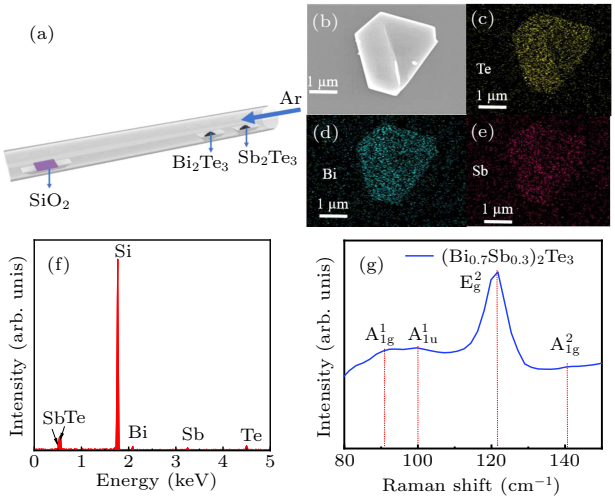


Fig. 1. (a) Schematic illustration of the CVD equipment. (b) SEM image of the $(Bi_{0.7}Sb_{0.3})_2Te_3$ nanoplate grown on SiO_2/Si substrate. (c)–(e) Elemental mapping of Te, Bi, and Sb of the $(Bi_{0.7}Sb_{0.3})_2Te_3$ nanoplate. (f) The EDS data of the $(Bi_{1-x}Sb_x)_2Te_3$ nanoplate. (g) Raman spectrum of the $(Bi_{0.7}Sb_{0.3})_2Te_3$ nanoplate.

Figure 2(a) shows the schematic drawing of the experimental setup for the HDPC measurement when the incident plane is perpendicular to the connection of the two contacts. Figure 2(b) shows the dependence of the photocurrent of the $(Bi_{0.7}Sb_{0.3})_2Te_3$ nanoplate on the quarter-wave plate angle φ measured under the geometry shown in Fig. 2(a). The incident angle is 30°, and the light power on the sample is 100 mW. The inset of Fig. 2(a) shows the optical image of the $(Bi_{0.7}Sb_{0.3})_2Te_3$ nanoplate device. Here, the angle φ is the angle between the polarization direction of the light and the optical axis of the quarter-wave plate.

The HDPC current of the $(Bi_{0.7}Sb_{0.3})_2Te_3$ nanoplate can be obtained by fitting the polarization-dependent photocurrent

to the following equation:[4,11]

$$J = J_{\mathrm{HDPC}} \sin 2\varphi + L_1 \sin 4\varphi + L_2 \cos 4\varphi + j_0. \quad (1)$$

Here J_{HDPC} is the amplitude of the HDPC current. L_1 and L_2 are the amplitude of photocurrent due to the linear photogalvanic effect (LPGE), caused by the asymmetric scattering of electrons due to phonons or defects.[2,4,18] j_0 is the polarization-independent photocurrent, induced by Dember effect or photovoltaic effect.[3,4] The solid symbols are the experimental data, and the solid line is the fitting curve by using Eq. (1). By fitting, we can obtain the J_{HDPC}, L_1, L_2, and j_0, which are represented by green dotted, orange dashed, blue dashed, and dashed-dotted lines, respectively, in Fig. 2(b).

HDPC has two origins, i.e., circular photogalvanic effect (CPGE) and circular photodrag effect (CPDE). The former one is due to the transfer of the angular momentum of the photon to the photo-generated carriers, while the latter one is owing to the transfer both of the angular momentum and the linear momentum of the photon to the photo-generated carriers.[11,19–22] The bulk states of $(Bi_{1-x}Sb_x)_2Te_3$ nanoplates belong to D_{3d} symmetry group, which will not generate CPGE current, and the CPGE current can only come from the surface states or the two-dimensional electron gas (2DEG) of the $(Bi_{1-x}Sb_x)_2Te_3$ nanoplates, which have a symmetry of C_{3v}.[1] By measuring the HDPC current under ionic liquid top-gate voltage, it is revealed that the HDPC is mainly contributed by the surface states rather than the 2DEG (see the discussion below). The bulk states and surface states of $(Bi_{1-x}Sb_x)_2Te_3$ nanoplates will also generate CPDE current, which has two components, named as $J^{\mathrm{I}}_{\mathrm{CPDE}}$ and $J^{\mathrm{II}}_{\mathrm{CPDE}}$, respectively. CPGE and CPDE currents show different dependences on incident angles, i.e., CPGE is proportional to $\sin\theta_0$, $J^{\mathrm{I}}_{\mathrm{CPDE}}$ and $J^{\mathrm{II}}_{\mathrm{CPDE}}$ are proportional to $\sin 2\theta_0$ and $\sin\theta_0^2$, respectively.[2,4,14] Therefore, we can distinguish their corresponding contributions to the HDPC by their different dependences on incident angles.

Figure 2(c) shows the dependence of the HDPC of the $(Bi_{0.7}Sb_{0.3})_2Te_3$ nanoplate on incident angle of light, when the incident plane is perpendicular to the connection of the two contacts. It can be seen that at this case, the HDPC shows an odd function on the incident angle, indicating that it is mainly contributed by J_{CPGE} and $J^{\mathrm{I}}_{\mathrm{CPDE}}$. Therefore, we fit the angle-dependent HDPC current by the equation of $J = C_1 \sin\theta_0 + C_2 \sin 2\theta_0 + J_{\mathrm{C0}}$. Here J_{C0} is the HDPC induced by the spin-polarized carriers with an out-of-plane spin due to the hexagonal warping effect of $(Bi_{0.7}Sb_{0.3})_2Te_3$. The fitting curve is shown by the solid line in Fig. 2(c). By fitting we can separate the contributions of the J_{CPGE} and $J^{\mathrm{I}}_{\mathrm{CPDE}}$ to the total HDPC, and the J_{CPGE} and $J^{\mathrm{I}}_{\mathrm{CPDE}}$ obtained by fitting is indicated by the dashed-dotted and dotted lines, respectively. By fitting, we obtain C_1 is 0.882 nA, and C_2 is 0.015 nA, suggesting that the HDPC is mainly contributed by the J_{CPGE}, which takes up 98% of the total HDPC current. In the following discussion, we will use the term "CPGE" instead of "HDPC", when the incident plane is perpendicular to the incident plane.

The CPGE normalized by the light power and light spot area observed in the 30-nm thick $(Bi_{0.7}Sb_{0.3})_2Te_3$ nanoplate is about 6.37 nA/(W·mm^2), which is at the same level with that observed in the 7-nm thick Bi_2Se_3 nanoplate (about 7.07 nA/(W·mm^2)) reported in our previous work.[16] The Bi_2Se_3 nanoplate reported in Ref. [16] had the similar device area with that of the $(Bi_{0.7}Sb_{0.3})_2Te_3$ nanoplate.

Figure 3(a) shows the experimental geometry for measuring the HDPC of the $(Bi_{0.7}Sb_{0.3})_2Te_3$ nanoplate when the incident plane is parallel to the connection of the two contacts. Figure 3(b) displays the dependence of the HDPC on the incident angle under the geometry shown in Fig. 3(a). It can be seen that, under this case, the HDPC shows an even function dependence on incident angles, indicating that the HDPC is dominated by $J^{\mathrm{II}}_{\mathrm{CPDE}}$. The solid line is the fitting curve by using the equation of $J^{\mathrm{II}}_{\mathrm{CPDE}} = C_3 \sin^2\theta_0 + J_{\mathrm{C0}}$, which is in good agreement with the experimental data and suggests that the HDPC is indeed mainly contributed by $J^{\mathrm{II}}_{\mathrm{CPDE}}$.

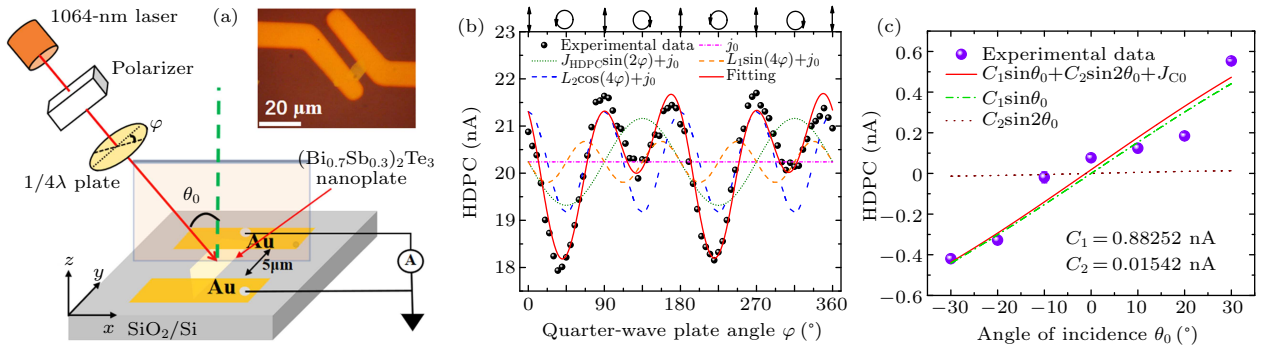


Fig. 2. (a) Schematic drawing of the experimental setup for the HDPC measurement when the incident plane is perpendicular to the connection of the two contacts. The inset shows the optical image of the $(Bi_{0.7}Sb_{0.3})_2Te_3$ nanoplate device. (b) Dependence of the photocurrent on the quarter-wave plate angle φ of the the $(Bi_{0.7}Sb_{0.3})_2Te_3$ nanoplate measured under the geometry shown in panel (a). The solid symbols are the experimental data, and the solid line is the fitting curve by using Eq. (1). The green dotted, orange dashed, blue dashed, and dashed-dotted lines represent $J_{\mathrm{HDPC}} \sin 2\varphi + j_0$, $L_1 \sin 4\varphi + j_0$, $L_2 \cos 4\varphi + j_0$, and j_0, respectively. (c) Dependence of the HPDC on the incident angle of light, when the incident plane is perpendicular to the connection of the two contacts.

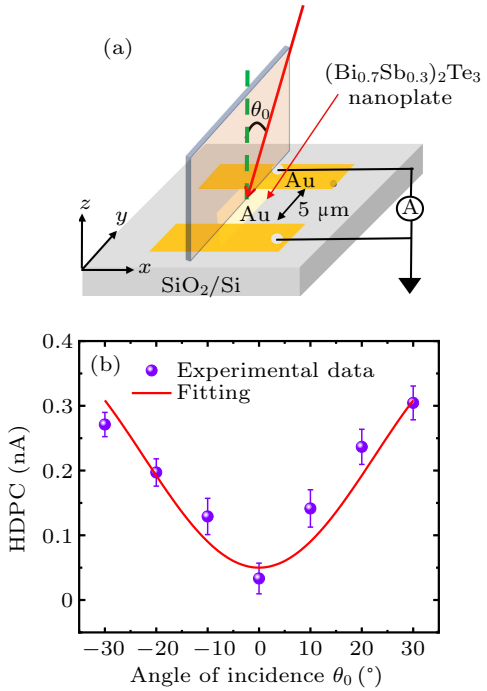


Fig. 3. (a) Schematic drawing of the experimental setup for the HDPC measurement when the incident plane is parallel to the connection of the two contacts. (b) Dependence of the HDPC on the incident angle of light, when the incident plane is parallel to the connection of the two contacts.

Figure 4(a) shows the power dependence of the CPGE for the $(Bi_{0.7}Sb_{0.3})_2Te_3$ nanoplate, which is measured under the geometry shown in Fig. 2(a) with θ_0 being 30°. The solid line is the linear fitting result. It can be seen that the CPGE almost linearly increases with the increasing of the light power, which can be attributed to the increase of the photo-generated carrier density as the increase of the light power.

Figure 4(b) displays the dependence of the CPGE on the source–drain voltage for the $(Bi_{0.7}Sb_{0.3})_2Te_3$ nanoplate, measured at θ_0 of 30° under an illumination of light power of 100 mW. As the source–drain voltage increases, the CPGE current also increases. The CPGE under a source–drain voltage can be expressed as[24]

$$I_{\mathrm{CPGE}} = \frac{\eta P\lambda}{Ahc}(\tau^{\sigma+}-\tau^{\sigma-})e\mu E + \frac{k\eta P\lambda}{Ahc}(\tau^{\sigma+}+\tau^{\sigma-})e\mu E^2. \quad (2)$$

Here, η is the optical absorption of the $(Bi_{0.7}Sb_{0.3})_2Te_3$ nanoplate under zero bias, and P is the light power. A is the area of illumination, and h is Planck's constant. c is the speed of light, e is the charge carried by an electron, and μ is the mobility of the carriers. $\tau^{\sigma+}$ (or $\tau^{\sigma-}$) is the lifetime of the photo-generated carriers generated by left-handed circularly polarized light σ^+ (or right-handed circularly polarized light σ^-). E is the electric field due to the applied source–drain voltage, and k is the constant related to the degree of the current-induced spin polarization (CISP). It can be seen from Eq. (2) that the CPGE under a source–drain voltage has two components, i.e., one is proportional to E, named as I^{I}_{CPGE}, the other is proportional to E^2, named as $I^{\mathrm{II}}_{\mathrm{CPGE}}$. I^{I}_{CPGE} can be attributed to the spin splitting due to the intrinsic or extrinsic SOC, while the $I^{\mathrm{II}}_{\mathrm{CPGE}}$ is due to the CISP. To separate these two components, we fit the source–drain voltage-dependent CPGE by the equation of $I_{\mathrm{CPGE}} = A_1V_{\mathrm{ds}} + A_2V_{\mathrm{ds}}^2 + I_{\mathrm{C0}}$. Here, I_{C0} is the CPGE current under zero bias, and A_i ($i = 1$ or 2) is the fitting parameter. The fitting result is shown by the solid line in Fig. 4(b), and the $I^{\mathrm{I}}_{\mathrm{CPGE}}$ and $I^{\mathrm{II}}_{\mathrm{CPGE}}$ obtained by fitting are shown by the dashed and dotted lines, respectively. It can be seen that the value of $I^{\mathrm{I}}_{\mathrm{CPGE}}$ and $I^{\mathrm{II}}_{\mathrm{CPGE}}$ are in the same order for the $(Bi_{0.7}Sb_{0.3})_2Te_3$ nanoplate.

The origin of $I^{\mathrm{I}}_{\mathrm{CPGE}}$ can be understood in this way. Without applying source–drain voltage, the CPGE can be expressed as $I_{\mathrm{C0}} = (\Delta n^{\sigma^+} - \Delta n^{\sigma^-})e\mu E_\alpha$. Here Δn^{σ^+} and Δn^{σ^-} are the photo-generated carrier density excited by the left-handed (σ^+) and right-handed (σ^-) circularly polarized light, respectively. The relation between Δn^{σ^+} (or Δn^{σ^-}) with $\tau^{\sigma+}$ (or $\tau^{\sigma-}$) can be expressed as $\Delta n^{\sigma^+} = (\eta P\lambda/(Ahc))\tau^{\sigma+}$ (or $\Delta n^{\sigma^-} = (\eta P\lambda/(Ahc))\tau^{\sigma-}$). μ is the mobility of the photo-generated carriers, and E_α is the equivalent electric field due to the SOC of the surface states. When applying a source–drain voltage V_{ds}, an external electric field E will be introduced, and the CPGE current can be written as $I^{\mathrm{I}}_{\mathrm{CPGE}} = (\Delta n^{\sigma^+} - \Delta n^{\sigma^-})e\mu(E_\alpha + E)$. Therefore, the CPGE current $I^{\mathrm{I}}_{\mathrm{CPGE}}$ will increase linearly with the source–drain voltage.

Figure 4(c) shows the dependence of the CPGE on the excitation wavelength for the $(Bi_{0.7}Sb_{0.3})_2Te_3$ nanoplate, measured at θ_0 of 30°. In this measurement, a mode-locked Ti:sapphire laser with a repetition frequency of 80 MHz is used as the light source, and the light power on the sample is 100 mW. It can be seen from Fig. 4(c) that the CPGE current increases as the wavelength of the laser changing from 700 nm to 1000 nm. It has been reported in Ref. [25] that, the optical absorption of $(Bi_{0.7}Sb_{0.3})_2Te_3$ decreases as the excitation wavelength increasing from 700 nm to 1000 nm. Therefore, the increase of the CPGE with increasing excitation wavelength cannot be attributed to the stronger optical absorption in longer wavelength. One possible reason for this phenomenon is that the excitation light with longer wavelength will lead to larger absorbed photon flux ϕ, since $\phi = \eta P\lambda/(Ahc)$.[20] As a result, the CPGE current increases with the increasing of the excitation wavelength.

Figure 5(a) shows the dependence of the CPGE on temperature for the $(Bi_{0.7}Sb_{0.3})_2Te_3$ nanoplate, measured at θ_0 of −30°. It can be seen that as the temperature decreases from 300 K to 77 K, the amplitude of the CPGE current increases. To find out the reason, we also measure the dependence of the photoconductance of the $(Bi_{0.7}Sb_{0.3})_2Te_3$ nanoplate on temperature with θ_0 of −30°. The measurement result is shown in Fig. 5(b). It can be seen that as the temperature decreases

from 300 K to 77 K, the amplitude of photoconductance also increases, which may be due to the increase of the mobility of the photo-generated carriers at low temperature. The same variation trend of the CPGE and photoconductance on temperature indicates that the dependence of the CPGE on temperature may be attributed to the same reason with that of the photoconductance, i.e., the variation of the photo-generated carriers and mobility with temperature.

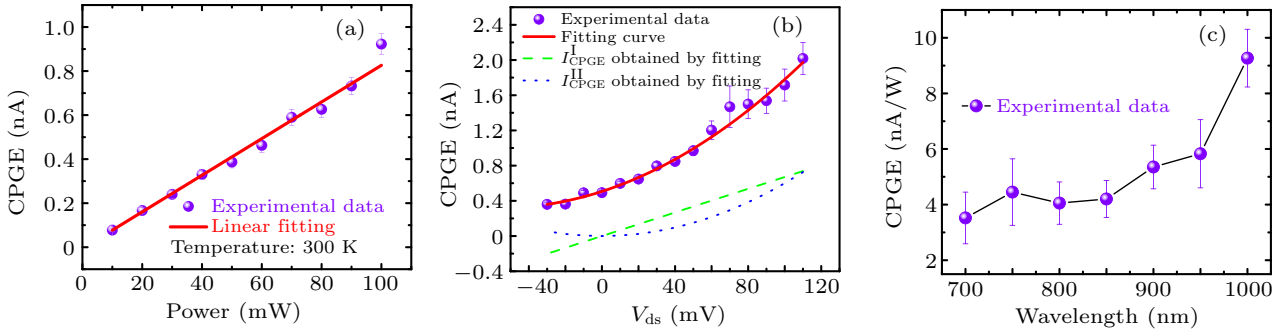


Fig. 4. (a) Dependence of the CPGE on the light power, measured at an incident angle of 30° at room temperature. (b) Dependence of the CPGE on the source–drain voltage of the $(Bi_{0.7}Sb_{0.3})_2Te_3$ nanoplate, measured at θ_0 of 30° under an illumination of light power of 100 mW. (c) Dependence of the CPGE on excitation wavelength for the $(Bi_{0.7}Sb_{0.3})_2Te_3$ nanoplate measured at θ_0 of 30°.

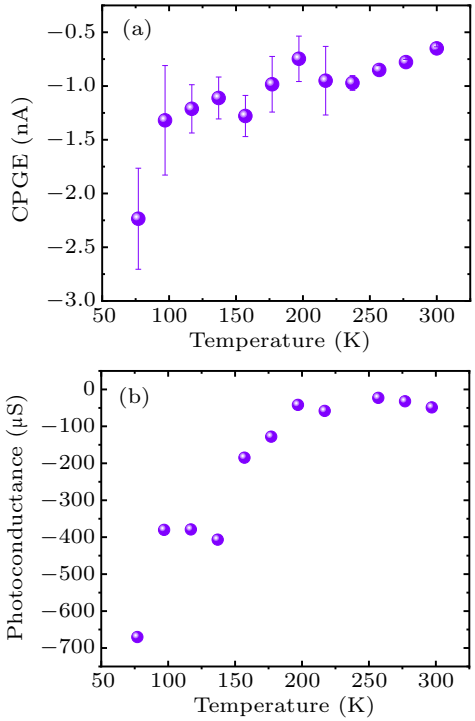


Fig. 5. (a) Dependence of the CPGE on temperature for the $(Bi_{0.7}Sb_{0.3})_2Te_3$ nanoplate measured at θ_0 of −30°. (b) Dependence of the photoconductance of the $(Bi_{0.7}Sb_{0.3})_2Te_3$ nanoplate on temperature.

Furthermore, we investigate the modulation of the CPGE current by applying ionic liquid top-gate voltage. The ionic liquid (DEME-TFSI) is dropped on the surface of the sample, and then covered by a quartz coverslip, as shown in Fig. 6(a). The gate voltage is applied between the gate and the $(Bi_{0.7}Sb_{0.3})_2Te_3$ nanoplate. The CPGE current is measured at an incident angle θ_0 of 30° under an illumination of 1064-nm light of 100 mW.

Figure 6(b) shows the dependence of the CPGE on the ionic liquid top-gate voltages for the $(Bi_{0.7}Sb_{0.3})_2Te_3$ nanoplate. It can be seen that, as the ionic liquid top-gate voltage V_g increases, the CPGE current decreases, and under the negative top-gate voltage, i.e., $V_g < 0$, the CPGE current increases. This is because the positive top-gate voltage will induce more electrons accumulating at the surface, leading to the further bending down of the energy band at the surface, as shown in the inset of Fig. 6(b). According to the previous works,[3,8] the electrons accumulating at the surface will generate two-dimensional electron gas (2DEG), which has an opposite spin-splitting with that of the top surface states of the topological insulator $(Bi_{0.7}Sb_{0.3})_2Te_3$. Therefore, the CPGE generated by the 2DEG will have opposite sign with that of the top surface states. As V_g increases, the SOC of the 2DEG also increases, leading to larger CPGE of the 2DEG. Besides, the positive top gate voltage will also make the Fermi level of the sample to move upward, as shown in the right inset of Fig. 6(b), which will lead to stronger scattering of the photo-generated spin-polarized carriers.[18] As a result, the CPGE generated by the surface states will decrease. In our experiments, the CPGE current decreases with the increasing of V_g, indicating that without applying top-gate voltage, the CPGE is dominated by the top surface states of the topological insulator.[8] Under negative top-gate voltage, the energy band at the surface will bend upward. This will lead to an SOC with the same sign with that of the top surface states, and it will generate CPGE current with the same sign with that of the top surface states. At the same time, the negative top-gate voltage will also move the Fermi level downward, as shown in the right inset of Fig. 6(b), leading to less scattering of the photo-generated spin-polarized carriers and larger CPGE current of the surface states.[18] As a result, the total CPGE current increases as the decreasing of the top-gate voltage.

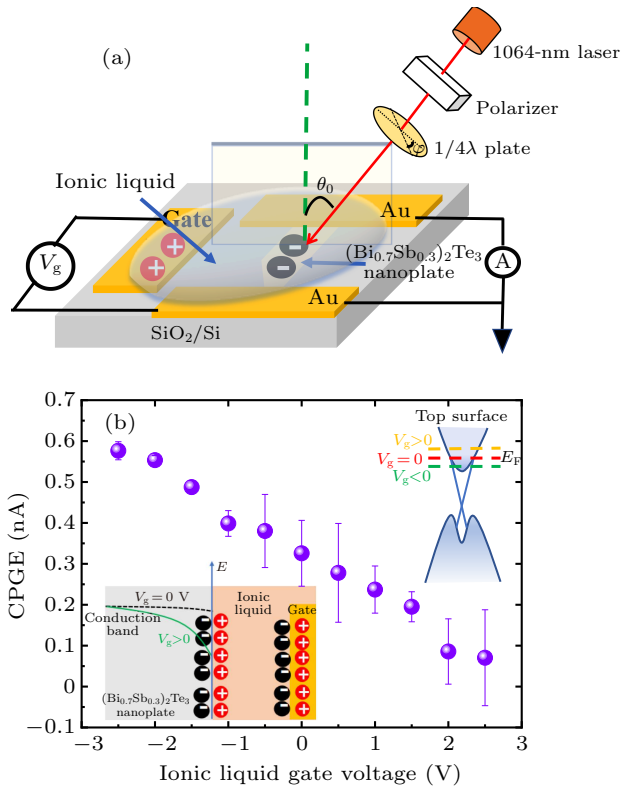


Fig. 6. (a) Schematic drawing of the experimental setup for the CPGE measurement when applying ionic liquid top-gate voltage. (b) Dependence of CPGE on the ionic liquid top-gate voltages for the $(Bi_{0.7}Sb_{0.3})_2Te_3$ nanoplate measured at θ_0 of 30°. The left inset shows the schematic drawing of electric double-layer transistor geometry formed by applying ionic liquid top-gate voltage, and the right inset displays the schematic diagram of the moving of the Fermi level under different top-gate voltages.

4. Conclusion

In summary, we have investigated the HDPC of the surface states in a $(Bi_{0.7}Sb_{0.3})_2Te_3$ nanoplate grown by CVD. It is demonstrated that the HDPC is mainly contributed by the CPGE when the incident plane is perpendicular to the connection of the two contacts, while the CPDE dominates the HDPC when the incident plane is parallel to the connection of the two contacts. The CPGE of the $(Bi_{0.7}Sb_{0.3})_2Te_3$ nanoplate increases almost linearly with excitation light power. As the excitation wavelength increases from 700 nm to 1000 nm, the CPGE current also increases. As the temperature decreases from 300 K to 77 K, the CPGE current increases, which shows the same trend with that of the photoconductance. Besides, the CPGE can also be effectively tuned by the source–drain and ionic liquid top-gate voltages. As the source–drain voltage increases, the CPGE current increases. The CPGE due to the intrinsic or extrinsic SOC and that due to the CISP effect is successfully separated. As the top-gate voltage increases, the CPGE current decreases, indicating that the CPGE of the $(Bi_{0.7}Sb_{0.3})_2Te_3$ nanoplate is dominated by the top surface states under zero bias. Our work suggests that $(Bi_{0.7}Sb_{0.3})_2Te_3$ nanoplates may provide good platforms for novel opto-spintronics devices.

Acknowledgements

Project supported by the National Natural Science Foundation of China (Grant Nos. 62074036, 61674038, and 11574302), the Foreign Cooperation Project of Fujian Province, China (Grant No. 2023I0005), the Open Research Fund Program of the State Key Laboratory of Low-Dimensional Quantum Physics (Grant No. KF202108), the National Key Research and Development Program of China (Grant No. 2016YFB0402303), and the Foundation of Fujian Provincial Department of Industry and Information Technology of China (Grant No. 82318075).

References

[1] Mciver J W, Hsieh D, Steinberg H, Jarillo-Herrero P and Gedik N 2012 *Nat. Nanotechnol.* **7** 96
[2] Olbrich P, Golub L E, Herrmann T, Danilov S N, Plank H, Bel'kov V V, Mussler G, Weyrich Ch, Schneider C M, Kampmeier J, Grutzmacher D, Plucinski L, Eschbach M and Ganichev S D 2014 *Phys. Rev. Lett.* **113** 096601
[3] Yu J, Zeng X, Zhang L, He K, Cheng S, Lai Y, Huang W, Chen Y, Yin C and Xue Q 2017 *Nano Lett.* **17** 7878
[4] Pan Y, Wang Q Z, Yeats A L, Pillsbury T, Flanagan T C, Richardella A, Zhang H, Awschalom D D, Liu C X and Samarth N 2017 *Nat. Commun.* **8** 1037
[5] Su S H, Chuang P Y, Lee J C, Chong C W, Li Y W, Lin Z M, Chen Y C, Cheng C M and Huang J A 2021 *ACS Appl. Electron.* **3** 2988
[6] Chen W 2020 *J. Phys. Condens. Matter* **32** 035809
[7] Bonell F, Goto M, Sauthier G, Sierra J F, Figueroa A I, Costache M V, Miwa S, Suzuki Y and Valenzuela S O 2020 *Nano Lett.* **20** 5893
[8] Mei F H, Tang N, Wang X Q, Duan J X, Zhang S, Chen Y H, Ge W K and Shen B 2012 *Appl. Phys. Lett.* **101** 132404
[9] Duan J, Tang N, He X, Yan Y, Zhang S, Qin X, Wang X, Yang X, Xu F, Chen Y, Ge W and Shen B 2014 *Sci. Rep.* **4** 4889
[10] Thanopulos I, Yannopapas V and Paspalakis E 2022 *Opt. Lett.* **47** 5240
[11] Chen S, Yu J, Hong X, Zhu K, Chen Y, Cheng S, Lai Y, He K and Xue Q 2023 *Photon. Res.* **11** 1902
[12] Bai Y, Li N, Li R and Liu P 2022 *Adv. Phys. X* **7** 2013134
[13] Nikoofard H, Esmaeilzadeh M, Farghadan R and Sun J T 2022 *Phys. Rev. B* **106** 165127
[14] Yu J, Zhu K, Zeng X, Chen L, Chen Y, Liu Y, Yin C, Cheng S, Lai Y and Huang J 2019 *Phys. Rev. B* **100** 235108
[15] Yu J, Xia L, Zhu K, Pan Q, Zeng X, Chen Y, Liu Y, Yin C, Cheng S and Lai Y 2020 *ACS Appl. Mater. Interfaces* **12** 18091
[16] Zhuang H, Yu J L, Chen L, Gu P, Chen Y H, Liu Y, Yin C M, Lai Y F and Cheng S Y 2021 *J. Appl. Phys.* **129** 105303
[17] Wu W, Yu J, Jiang Y, Zeng X, Chen Y, Liu Y, Yin C, Cheng S, Lai Y and He K 2022 *Appl. Phys. Lett.* **120** 062407
[18] Okada K N, Ogawa N, Yoshimi R, Tsukazaki A, Takahashi K S, Kawasaki M and Tokura Y 2016 *Phys. Rev. B* **93** 081403
[19] Urkude R R and Palikundwar U A 2023 *Physica B* **655** 414754
[20] Wu W, Yu J, Chen Y H, Liu Y, Cheng S, Lai Y, Sun J, Zhou H and He K 2023 *ACS Nano* **17** 16633
[21] Jiang C, Shalygin V A, Panevin V Y, Danilov S N, Glazov M M, Yakimova R, Lara-Avila S, Kubatkin S and Ganichev S D 2011 *Phys. Rev. B* **84** 125429
[22] Huang Y Q, Song Y X, Wang S M, Buyanova I A and Chen W M 2017 *Nat. Commun.* **8** 15401
[23] Bahramy M S, King P D, de la Torre A, Chang J, Shi M, Patthey L, Balakrishnan G, Hofmann P, Arita R, Nagaosa N and Baumberger F 2012 *Nat. Commun.* **3** 1159
[24] Yu J L, Zhuang H, Zhu K J, Chen Y H, Liu Y, Zhang Y, Yin C M, Cheng S Y, Lai Y F and He K 2021 *Phys. Rev. B* **104** 045428
[25] Yin J, Krishnamoorthy H N S, Adamo G, Dubrovkin A M, Chong Y, Zheludev N I and Soci C 2017 *NPG Asia Mater.* **9** e425